ACS OMEGA

Open Access

http://pubs.acs.org/journal/acsodf

Article

Electrospun Nanofibrous UV Filters with Bidirectional Actuation Properties Based on Salmon Sperm DNA/Silk Fibroin for Biomedical Applications

Maria Rachele Ceccarini, Irene Chiesa, Francesca Ripanti, Martina Alunni Cardinali, Simone Micalizzi, Gabriele Scattini, Carmelo De Maria, Alessandro Paciaroni, Caterina Petrillo, Lucia Comez, Matteo Bertelli, Paola Sassi, Luisa Pascucci, Tommaso Beccari, and Luca Valentini*

Cite This: *ACS Omega* 2023, 8, 38233−38242

Read Online

ACCESS | Metrics & More | Article Recommendations | Supporting Information

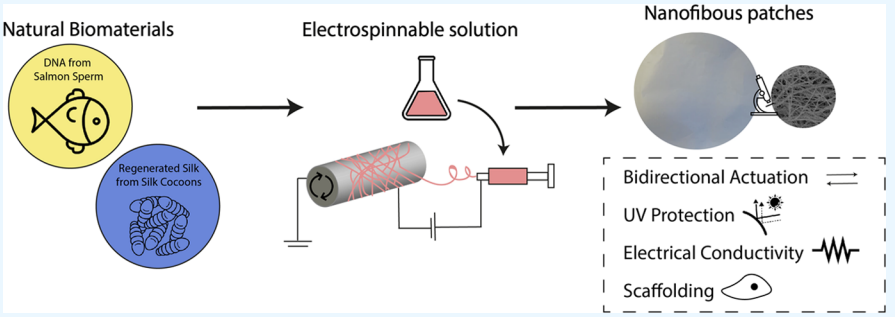

ABSTRACT: In this study, we dissolved *Bombyx mori* degummed silk [i.e., silk fibroin (SF)] and salmon sperm deoxyribonucleic acid (DNA) in water and used a bioinspired spinning process to obtain an electrospun nanofibrous SF-based patch (ESF). We investigated the bidirectional macroscale actuation behavior of ESF in response to water vapor and its UV-blocking properties as well as those of ESF/DNA films. Fourier transform infrared (FTIR) results suggest that the formation of β-sheet-rich structures promotes the actuation effect. ESF/DNA film with high-ordered and β-sheet-rich structures exhibits higher electrical conductivity and is water-insoluble. Given the intrinsic ability of both SF and DNA to absorb UV radiation, we performed biological experiments on the viability of keratinocyte HaCaT cells after exposure to solar spectrum components. Our findings indicate that the ESF/DNA patch is photoprotective and can increase the cellular viability of keratinocytes after UV exposure. Furthermore, we demonstrated that ESF/DNA patches treated with water vapor can serve as suitable scaffolds for tissue engineering and can improve tissue regeneration when cellularized with HaCaT cells. The 3D shape morphing capability of these patches, along with their potential as UV filters, could offer significant practical advantages in tissue engineering.

INTRODUCTION

Once spiders and silkworms release their silk proteins from the spinneret, they undergo an instantaneous solidification process in nature.[1−4] Replicating the physiological and environmental conditions necessary for the solidification of silk proteins, as observed in spiders and silkworms, is challenging under laboratory conditions. Several studies have reported various spinning processes,[5−13] where the silk protein solidification takes place either in a coagulation bath or through the evaporation of a volatile solvent.

Beyond the natural solidification mechanism of animal-derived silks, it is also known that silk, when wetted, shrinks with radial swelling;[14−17] the involvement of water molecules in this process is critical as they play a crucial role in disrupting the hydrogen bonds within the noncrystalline regions. Thus, water molecules facilitate the transition of these regions into lower energy configurations.[18−20] This contraction mechanism can be mimicked by multilayer polymeric films that actuate upon exposure to heat, moisture, and solvent vapors.[21−28] A major limitation of this approach is the use of multiple polymer films, which not only complicates the actuator system but also compromises its durability. Moreover, the challenge of effectively integrating these materials into biological tissues is often overlooked. In light of this, there is a growing demand for soft actuators that are based on biopolymers, as they offer a valuable solution for biomedical devices and smart biocompatible substrates.[29,30]

Received: June 26, 2023
Accepted: August 23, 2023
Published: October 4, 2023

https://doi.org/10.1021/acsomega.3c04563
ACS Omega 2023, 8, 38233−38242

Therefore, spinning biopolymers consisting of natural proteins could attract attention as a method to fabricate films with multifunctional properties. In nature, there are several proteins displaying water vapor responsiveness that undergo different swelling/shrinkage profiles[31] as well as UV-blocking properties.[32] An intriguing possibility could be to exploit the synergistic effect of different biomaterials for bending, helixing, and twisting transformations of planar architecture with intrinsic UV-shielding properties for 3D biomedical scaffolds.

In this framework, deoxyribonucleic acid (DNA) and silk fibroin (SF) are inexhaustible natural polymers that can be extracted from living organisms.[33,34] DNA is water-soluble and has UV-absorption ability, while SF can form crystalline domains with a β-sheet conformation. Taking advantage of these intrinsic properties of SF and DNA, in a recent study,[35] we reported the fabrication of adhesive films with UV-blocking properties, starting from the dissolution of silk fibers and salmon sperm DNA in calcium chloride ($CaCl_2$)/formic acid solution. However, it is known that the mechanical properties of silk are due to its hierarchical fibrillar structure.[1,36] A more sustainable approach to preserve the fibrillar structure can be achieved using a conventional dissolving system. This involves the gradually increase of the SF solution concentration and allows ample time for the self-assembly of the nanofilaments in water. By employing this method, the desired fibrillar structure can be effectively maintained while promoting sustainability. Moreover, the toxicity of formic acid limits the electrospinning of silk fibers in a laboratory.[37] Here, based on the observation of the natural dry-spinning described above, we set up a bioinspired spinning strategy at ambient conditions to collect regenerated silk modified with salmon sperm DNA in a water environment by electrospinning lyophilized SF/DNA in hexafluorophosphoric (HIFP) acid solution and pulling the electrospun silk fiber (ESF).[38]

We demonstrated that the as-prepared nanofibrous patches can be used to shield skin cells from UV exposure. The resultant nanofibrous electrospun patch also demonstrated bidirectional actuation upon exposure to water vapor and, crucially, remained insoluble even after being exposed to water molecules, making it suitable for being cellularized with HaCaT cells. The sustainable and biocompatible properties of regenerated SF and DNA make them appealing platforms for future biomedical devices.

MATERIALS AND METHODS

Materials. Silk cocoons were supplied by a local farm (Fimo srl, Milano, Italy), while sodium hydrogen carbonate ($NaHCO_3$), lithium bromide, and hexafluorophosphoric acid (HIFP) were provided by Merck (Darmstadt, Germany). Salmon sperm DNA (double-stranded DNA, molecular weight = 5×10^3 g/mol, 23 base pairs) was purchased from Merck (Darmstadt, Germany). Human keratinocytes (HaCaT cell lines) were purchased from IZSLER from the Istituto Zooprofilattico Sperimentale della Lombardia e dell'Emilia Romagna "Bruno Ubertini" (Brescia, Italy). Cells were grown in 75 cm^2 tissue flasks with Dulbecco's modified Eagle medium (DMEM) medium supplemented with 100 U/mL penicillin, 100 μg/mL streptomycin, 2 mM L-glutamine, and 10% fetal bovine serum (FBS) under a humidified atmosphere of 5% CO_2 at 37 °C.

Preparation of SF/DNA Solutions. The water solution of SF was obtained according to a standard protocol.[37] Briefly, the process involved in preparing the SF/DNA samples can be outlined as follows: *Bombyx mori* silk cocoons (10 g) were boiled in 200 mL of water containing 5 g of $NaHCO_3$ for 30 min, and then the extracted silk fibers were washed twice with water and dried at room temperature in a chemical hood with laminar flow. The degummed silk fibers were then dissolved in a 9.3 M lithium bromide solution at 60 °C for 4 h. The silk solution was dialyzed to remove the lithium bromide, resulting in a silk solution with a concentration of approximately 7.5 wt %. Finally, the silk solution was stored at 4 °C before use. Five DNA mixtures were prepared by mixing in water different DNA concentrations (1.3 mg/mL, 2 mg/mL, 2.6 mg/mL, 3.3 mg/mL, and 4 mg/mL, respectively). Then, 0.4 mL of the DNA water solution was added into 5 mL of silk solution; SF/A, SF/B, SF/C, SF/D, and SF/E refer to SF/DNA samples prepared by adding the five concentrations of DNA to the SF water solution.

Fabrication Protocol. SF, SF/B, and SF/E (i.e., the sample with the highest UV absorption as shown below) solutions were lyophilized (BenchTop Pro-SP Scientific) at −60 °C for 24 h and subsequently resuspended in HIFP on a stirring plate for 24 h at room temperature with a final concentration of 5% w/v.

The electrospinning process was performed using a Linari Engineering apparatus (Linari Eng, Italy) featuring a custom-made cylindrical rotating spindle (rpm = 800) covered with an aluminum foil as a grounded collector, and a commercial 10 mL syringe with 21 G (outer diameter = 0.81 mm, inner diameter = 0.51 mm) needle as spinneret.[37] The applied voltage was set to 30 kV; the distance between the spinneret and the grounded collector was set to 10 cm; and the flow was set to 1 mL/h. The electrospinning process was conducted for 4 h at room temperature. Subsequently, the aluminum foil with the electrospun materials was stored for 24 h at room temperature for completing the drying process. Then, the electrospun patches were removed from the aluminum foil and kept at room temperature for further use.

ESF and ESF/DNA nanofibrous patches were treated with water vapor in order to achieve solvent-induced crystallization of fibroin. Briefly, water vapor-treated samples were prepared by fixing ESF and ESF/DNA patches into a plexiglass mold with three pairs of elliptical holes, 0.6 cm deep, with dimensions of 1.1 cm × 0.5 cm and exposed to saturated water vapor at 50 °C for 30 min and then dried at room temperature.

Materials and Patches Characterization. To assess the spectral absorption and the structure of SF, DNA, and SF/DNA solutions, UV−vis absorption experiments and circular dichroism (CD) measurements were performed. Solutions of SF, DNA, and SF/DNA were measured in a quartz cuvette of a 1-mm optical path. A Jasco V-570 spectrophotometer, in the spectral range from 200 to 350 nm, was used for the UV−vis absorption while CD experiments were carried out with a Jasco J-810 spectropolarimeter in the 200−350 nm spectral range, with a 50 nm/min scan speed.

Infrared spectra of the electrospun patches were collected using a Fourier transform Alpha spectrometer from Bruker Optics and its ATR (attenuated total reflection) module equipped with a diamond crystal. The spectra were gathered in the 5000−300 cm^{-1} spectral range with 30 scans and an average resolution of 2 cm^{-1}.

Comparative experiments of the electrical conductivity of ESF and ESF/DNA rectangular patches were performed by inserting them into the plexiglass mold and fixing between two stripes of adhesive copper. The current−voltage characteristics during the exposure to water vapor were recorded by a Keithley 4200 SCS. The voltage sweep was performed between −1 and 1 V.

https://doi.org/10.1021/acsomega.3c04563
ACS Omega 2023, 8, 38233−38242

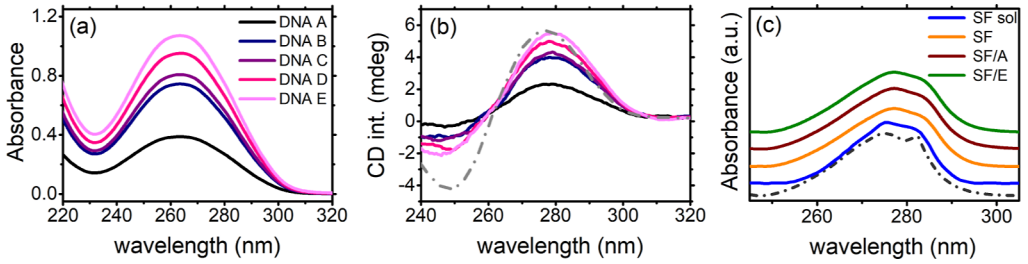

Figure 1. (a) UV−vis and (b) CD spectra of DNA solution at different concentrations. The dash dotted line represents the CD profile of B-DNA,[39] reported here for comparison. (c) UV−vis spectra of SF solution (blue) compared to that already present in literature[40] (dash dotted line) and to that obtained from SF film (orange). Selected spectra of SF/DNA films (SF/A wine and SF/E green) are also reported for comparison. Spectra are vertically shifted for the sake of clarity.

The surface morphology of the electrospun films was investigated by a field-emission scanning electron microscopy (FESEM) (UHR FE-SEM FIB TESCAN AMBER X) with an energy of 2 keV at a working distance of 4.89 mm. Moreover, from the obtained images, the distribution of the nanofiber dimensions was investigated via image analysis using the DiameterJ plugin of Fiji.

The actuation characteristics of ESF and ESF/DNA patches upon exposure to the water vapors were investigated by setting the distance between the top surface of the water bath and the bottom surface of the patch to about 10 mm. Images of the sample actuation were acquired with a camera and analyzed with ImageJ to obtain the radius of curvature of the structure. Briefly, after setting the correct scale and cropping the image, nine points on the structure curvature were selected and the fit circle function was used to obtain the circle that better fits the selected points (Figure S1). Then, the measure function was used to get the perimeter of the circle, from which the radius could be obtained. Finally, the radius of the fitting circle was set to be equivalent to the radius of curvature of the patch.

The solubility in water of the vapor-treated patches was studied by measuring the weight variation between the initial (W_0) and soaked (W_s) weights in phosphate buffered saline (PBS, pH 7.5 at room temperature) after 1 week.

Irradiation, MTT Assay, and Scanning Electron Microscopy. HaCat cells were seeded in 35 mm dishes, at different concentrations: 1×10^4 cells/cm^2, 5×10^3 cells/dish, 2.5×10^3 cells/dish and after 4, 24, and 48 h, respectively, of incubation after 220 s of irradiation. Cell viability was calculated as previously described in ref 35.

First of all, human keratinocyte cell lines were harvested and seeded in DMEM supplemented with 10% of FBS (0.1% of antibiotics) (Pen/Strep); after 24 h, the medium was removed and two washes for each dish with prewarmed PBS (1X) 0.1 mM (137 mM NaCl, 2.7 mM KCl, 10 mM Na_2HPO_4, and 1.8 mM KH_2PO_4) pH 7.4 were carried out. 1 mL of PBS 1X was added to each dish to perform the irradiation. Cells were irradiated in prewarmed PBS 1X in air at room temperature with a 300 W xenon light (ThermoOriel solar simulator model 69907). The average power in a 33 mm diameter output beam in the wavelength range of UVC (230−280 nm), UVB (280−320 nm), UVA (320−400 nm), and Vis-nIR (400−780 nm) were 11.5 mW, 27 mW, 85 mW, and 430 mW, respectively. The doses of radiation during 220 s exposure were 2.96 kJ/m^2 (UVC), 6.95 kJ/m^2 (UVB), 21.9 kJ/m^2 (UVA), and 110 kJ/m^2 (Vis-nIR), respectively. PBS maintains the cells in suitable conditions for their life during radiation exposure; in addition, it is a transparent substance that does not absorb in the UV−vis spectrum. Negative control (CTR−) was kept in PBS 1X for the same time (220 s) as irradiated samples. Positive control (CTR +) was kept under the solar spectrum without any protection. After vapor treatment, ESF and ESF/DNA patches were used to cover the upper part of the dish (likewise a lid), so that the cell monolayer was protected against the rays. Each dish was irradiated for 220 s with a Thermo Oriel 66907 lamp, corresponding approximately to 1.5 h of sun exposure to UV-B rays. Immediately after irradiation, PBS 1X was removed, and 1 mL of complete DMEM was added to each dish. The cells were incubated at 37 °C and 5% of CO_2, and after 4, 24, 48 h of incubation, MTT assay was carried out to evaluate cell viability. MTT reagent was freshly prepared, and the final concentration was 5 mg/mL in PBS 1X. 100 μL of MTT was added to each dish in the final concentration of 0.5 mg/mL. After 3 h at 37° and 5% of CO_2, the supernatant and even the residual drops were eliminated. 1 mL of dimethyl sulfoxide was added for each dish to lyse the cells (30 min at 37 °C). The suspension was transferred into a 96-well plates and, at the end, the absorbance was measured at 540 nm by a spectrophotometer (ELIZA MAT 2000, DRG Instruments, GmbH). The experiments were performed twice in triplicate. The degree of viability can be expressed with the following formula

$$\text{Viable cells (\%)} = (\text{OD\_sample}/\text{OD\_CTR} -) \times 100$$

where OD is the optical density.

The same irradiation conditions were used to visualize the morphology of the HaCat cells with methylene blue staining. After 24 h of UV irradiation (220 s), HaCat cells were washed twice with PBS 1X and fixed by adding 300 μL of fixing solution for 10 min. After that two washes with PBS 1X were done, and cells were stained with 500 μL of methylene blue solution (Hank's balanced salt solution −HBSS +1.25% glutaraldehyde +0.6% methylene blue). After 10 min of incubation, dishes were washed twice with PBS 1X and finally rinsed with distilled water to remove salt residues.

To investigate the scaffolding properties of the ESF/E sample, SEM was performed. Prior to cell seeding, nanofibrous patches were sterilized for 30 min under UV light. Subsequently, nanofibrous patches were placed for 24 h in 24-well plates containing 0.5 mL of DMEM and HaCat cells were seeded on the top face of each patch at a final concentration of 1×10^5/cm^2 (total volume 50 μL) and incubated at 37 °C with 5% of CO_2. After 3 h, 1 mL of complete culture medium was added to each well and the patches were incubated for 24 h. Unseeded ESF/E was used as a control. Unseeded and HaCat seeded ESF/E were washed twice in PBS 1X for 10 min each and then fixed with 2.5% glutaraldehyde (Agar Scientific, UK) in phosphate buffer (PB) 1X for 1 h at RT. After fixation, patches were washed in PB

https://doi.org/10.1021/acsomega.3c04563
ACS Omega 2023, 8, 38233−38242

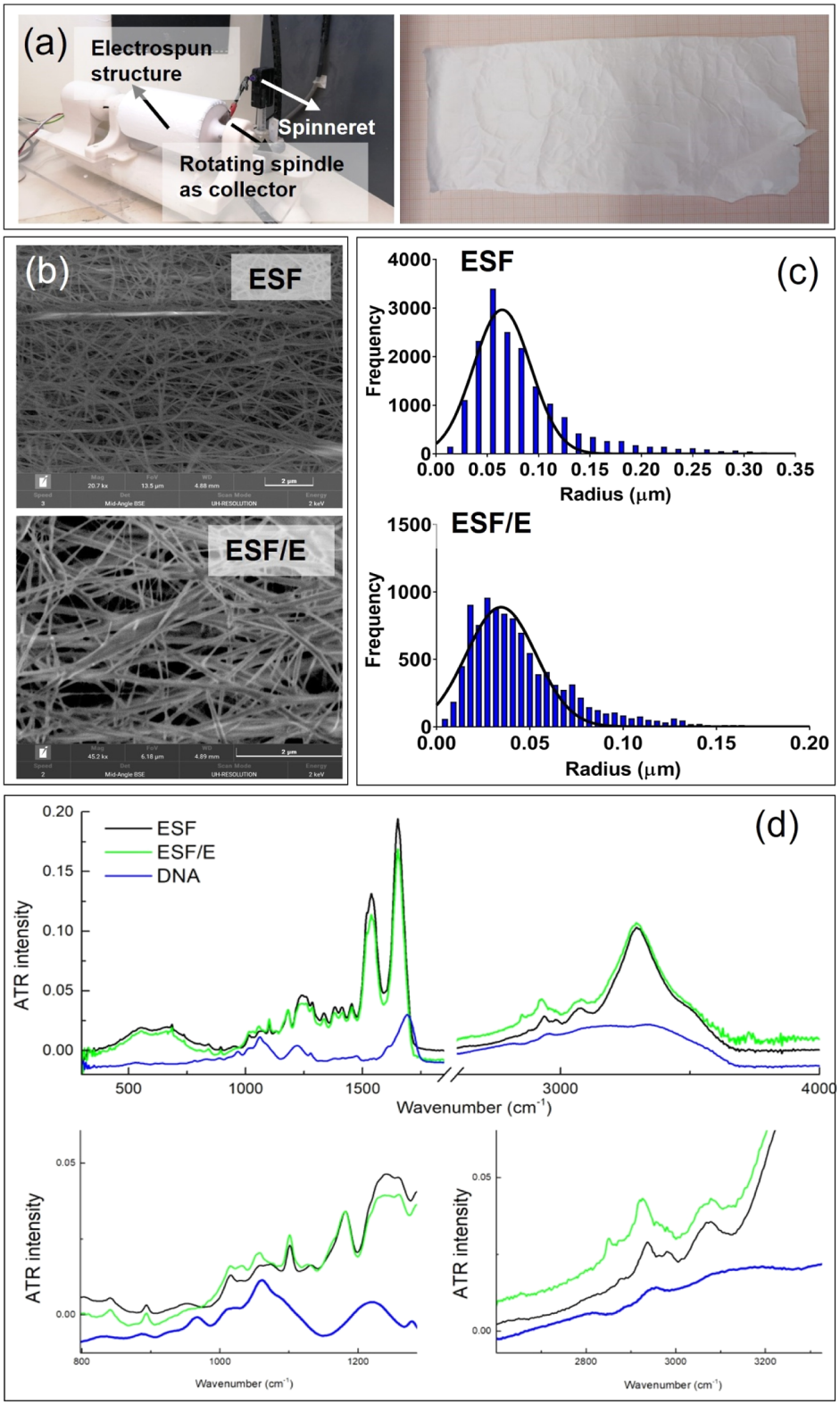

Figure 2. (a) Illustration of the electrospinning experimental setup and digital image of ESF patch. (b) FESEM images of ESF and ESF/E electrospun nanofibrous patches. (c) Statistical analysis of the fiber diameter distribution of ESF and ESF/patches. (d) ATR-FTIR spectra of ESF and ESF/E electrospun nanofibrous patches. ATR-FTIR spectrum of DNA was added for a comparison purpose.

1X and dehydrated in the graded series of ethanol up to absolute and air-dried.

ESF/E scaffolds with or without HaCat cells were placed on metal stubs and coated with chromium to a thickness of 15 nm. Images were acquired using the LEO 1525 Zeiss scanning electron microscope (L.U.N.A Laboratory, University of Perugia).

Statistical Analysis. GraphPad Prism 9.2.0.332 (GraphPad Software, San Diego, CA, USA) was used to assess the statistical significance of all the comparison studies in this work. In the

https://doi.org/10.1021/acsomega.3c04563
ACS Omega 2023, 8, 38233−38242

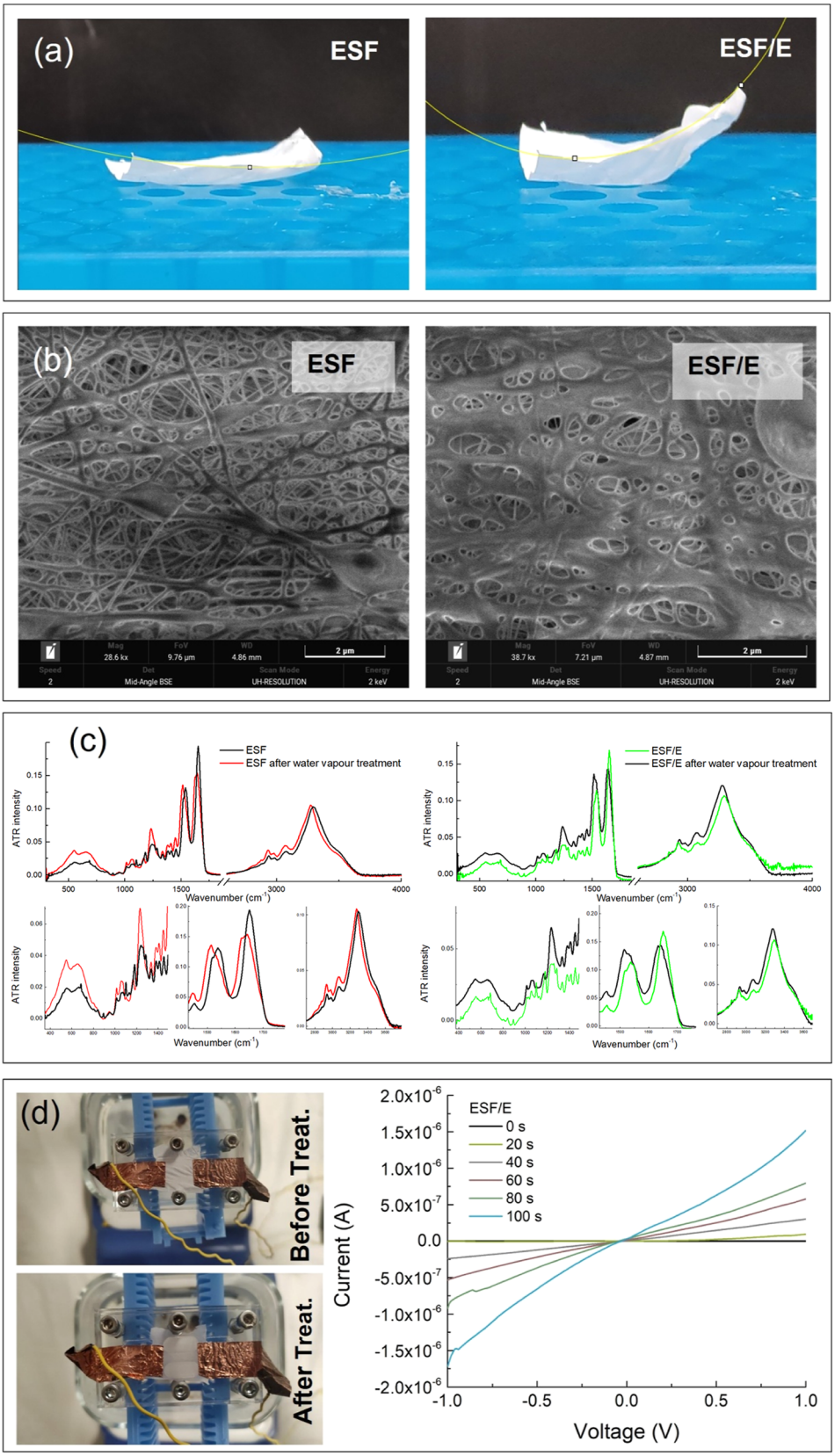

Figure 3. (a) Snapshots showing the ESF/E patch in an actuated state (bidirectional bending). (b) FESEM image of ESF and ESF/E electrospun nanofibrous patch after exposure to water vapor. (c) ATR-FTIR spectra of ESF and ESF/E electrospun nanofibrous patches after exposure to water vapor. (d) Photograph of the setup used to monitor the electrical conductivity vs crystallization time and evolution of current−voltage curves of ESF and ESF/E electrospun nanofibrous patches upon exposure to water vapor.

https://doi.org/10.1021/acsomega.3c04563
ACS Omega 2023, 8, 38233−38242

statistical analysis for comparison between multiple groups, a two-way ANOVA with Tukey's post hoc analysis (multiple comparisons) was conducted with the significance threshold of $*p < 0.05$, $**p < 0.01$, $***p < 0.001$, and $****p < 0.0001$.

RESULTS AND DISCUSSION

The UV absorption spectra of the DNA-former solutions are presented in Figure 1a, wherein it is evident that the maximum absorption at around 260 nm intensifies with an increasing concentration of the solution. The CD spectra of the same samples are shown in Figure 1b, with a minimum at around 245 nm and an intense maximum at around 280 nm, which are the typical features of the B-form DNA.[39] This indeed suggests that the main structure of the employed DNA solutions is the B-form. We observed that the DNA retains this structure also when inserted in the SF matrix, as reported in a previous work.[35] Moreover, UV−vis spectra of the initial SF/DNA solutions and films were measured and compared, as shown in Figure 1c. The absorption spectrum of SF film appears to be very similar to that of the native solution.[40] Additionally, the spectra of SF/DNA films exhibit very similar features among themselves (for the sake of clarity, we have included the results for the SF/A and SF/E samples). We also observe that the absorption spectrum is mainly dominated by the contribution of fibroin, which is, for example, at a concentration ≈1000 times higher than DNA for the SF/E sample.

Then, electrospinning equipped with a custom rotating spindle (Figure 2a) was used to fabricate nanofibrous patches with SF and SF/E solutions. The field emission scanning electron microscopy (FESEM) analysis of the electrospun patch was used to investigate the morphological changes of ESF nanofibers following the DNA addition. The addition of DNA does not significantly affect the morphology and dimension of the nanofibrous patch (Figure 2b,c). Indeed, the analysis of the fiber dimensions revealed that the fiber radius is around 50 nm for both solutions with a slightly more spread distribution for the SF/E patch (Figure 2c). Previous studies indicate that silk nanofibril is a semicrystalline polymer consisting of orientated nanocrystalline β-sheets embedded in an "amorphous" matrix.[41,42] We therefore investigated the FTIR absorption bands of ESF after the addition of DNA (Figure 2d). According to a recent study reported by Asakura,[43] the absorption bands at 1652 cm^{-1} (amide I) and 1540 cm^{-1} (amide II) of the ESF film can be attributed to the disordered conformation of silk fibroin. He suggested that, although the maximum of IR amide I band is observed at 1655 cm^{-1} (a frequency usually characteristic of α-helix conformation), the structure of the protein is of β-turn type.[43] In this regard, the second derivative profile of our ATR spectrum (see Figure S2) evidences two main contributions to the amide I band at 1647 and 1662 cm^{-1}, and also to the amide II bands with corresponding peaks at 1552 and 1534 cm^{-1}; this better clarifies the assignment of fibroin conformation to disordered/β-turn structures.[44]

The sharp DNA band at 1055 cm^{-1} is related instead to the C−O deoxyribose backbone motion of DNA.[45] To better identify this feature, we subtracted the ESF spectrum from that of ESF/E (Figure S2). The result shows that the profile contains much more highly resolved signals than the DNA spectrum; this could be due to the presence of a higher amount of water in the pure DNA sample, as evidenced by the presence of the broad absorptions at 3000−3500 cm^{-1} (see Figure 2d) and at 1560−1750 cm^{-1} (blue curve of Figure S2). Despite these differences and the low signal/noise ratio, the difference spectrum shows the main peaks in the 1000−1100 cm^{-1} and 1580−1750 cm^{-1} regions, which are compatible with those of DNA.[45,46]

The vapor-responsive behavior of ESF and ESF/E patches upon exposure to water vapor is reported in Figure 3a. The curvature is estimated by fitting a circle on the patch curvature by image analysis through ImageJ software. This analysis revealed that the inclusion of the DNA in the silk formulation decreased the radius of curvature and the actuation time. Indeed, a radius of curvature approximately equal to 9.8 cm reached in about 10 min was achieved by the ESF patch. Differently, a radius of curvature of approximately 3.5 cm reached in about 1.5 min was achieved by the ESF/E patch. While the upward bending of the patch upon exposure to water vapor can be rationalized by considering the differential swelling of the SF across the thickness leading to a stress gradient,[47−49] the contraction behavior is due to the relaxation of the structure to the coiled one when high relative humidity triggers the structural glass transition.[50,51] These patches, after being exposed to water vapor, became transparent (see Figure 3d), and during this process, the nanofibrils aggregate, leading to a less porous patch, making this effect more evident in the ESF/E sample (Figure 3b). ESF and ESF/E patches, after the water vapor treatment, were then immersed in PBS for 1 week. After being dried, the patches did not show significant variation of the original weight (Figure S3). The insolubility in PBS is compatible with that observed for SF films prepared from aqueous LiBr solution.[52] The vapor treatment initiates the structural transition to crystalline β-sheet inhibiting nanofibril dissolution. The FTIR spectra in Figure 3c show that the water vapor treatment has a marked effect on the structure of the protein (e.g., ESF and ESF/E samples) that is monitored not only by amide I, amide II, and amide III bands (at about 1650, 1540, and 1240 cm^{-1}, respectively), but it is also correlated with the redshift of amide A band at 3296 cm^{-1}, which is mostly (95%) related to the N−H stretching of the amide group and is very sensitive to the H-bond interactions on NH functionality. The redshift to 3276 cm^{-1} indicates that H-bond interactions on NH groups have been strengthened during the transition to the ordered β-structure.

The changes in the secondary structure of ESF induced by water-guided crystallization, as observed in the FTIR spectra, are related to the activation energy of the Arrhenius equation describing the time dependence of the DC electrical conductivity.[53] Hence, we monitored the intrinsic protein reaggregation by recording the variation of electrical conductivity (Figure 3d). In the case of the ESF patch, during the crystallization, we did not observe any variation of the electrical conductivity (Figure S4). From these results, we can see that the electrical conductivity discriminates between the two species due to the absence (oligomers) and presence (fibrils) of Arrhenius-like resistivity (Figure 3d). These findings could open up new perspectives for monitoring the aggregation of human proteins because of their involvement in protein misfolding diseases.

HaCaT cells were exposed to combinations of spectral bands from 230 to 700 nm for 220 s irradiation time. Based on the obtained results, both from viability (measured by MTT test) and morphology, it could be assumed that the ESF/DNA patch has a strong protective effect on HaCat cells during irradiation. In fact, as previously reported,[54] the combination of complete solar light containing UV, vis, and nIR light induced an important damage on human skin cells,[55] which is responsible of cytotoxicity and cell death.[56]

https://doi.org/10.1021/acsomega.3c04563
ACS Omega 2023, 8, 38233−38242

As a proof of principle, after 220 s of irradiation with Thermo Oriel 66907 lamp, the cells without protection start to produce reactive oxygen species, such as H_2O_2, and pro-inflammatory cytokines (e.g., IL-8 and IL-16) and continue with other physiological mechanisms that trigger mitochondrial and nuclear DNA damage[57] and, in the end, lead to cellular death. Using MTT assay, we verified HaCat viability after 220 s of irradiation without any types of protection (CTR+) and we observed (Figure 4a, in red) a gradual decrease just after 4 h ($p < 0.05$), but a strong worsening after 24 and 48 h postirradiation ($p < 0.0001$). On the contrary, the cell viability with ESF and ESF/DNA patches 4- and 24-h postirradiation remained similar to negative CTR (CTR−, Figure 4a, in black), which means no cytotoxic effect was registered. It is interesting to observe that 48-h postirradiation the ESF/E patch protection (Figure 4a, in blue) is higher than that obtained by using ESF and ESF/B patches. To confirm these results, we performed morphological analysis of HaCat cells after irradiation with and without patch protection (Figure 4b). Also, in this case, we confirmed that ESF/DNA was able to suppress biochemical UV-induced cell damage due to its UV-blocking activity. The shape of CTR− and ESF/DNA cells looked very similar in comparison with CTR+, which instead appeared smaller and crumpled with cytoplasmic retraction (peculiar to necrotic cells). Moreover, in terms of numbers, cells covered and protected with ESF/DNA were the same as CTR-. Taken together, these data suggest that this innovative patch could be used for skin protection.

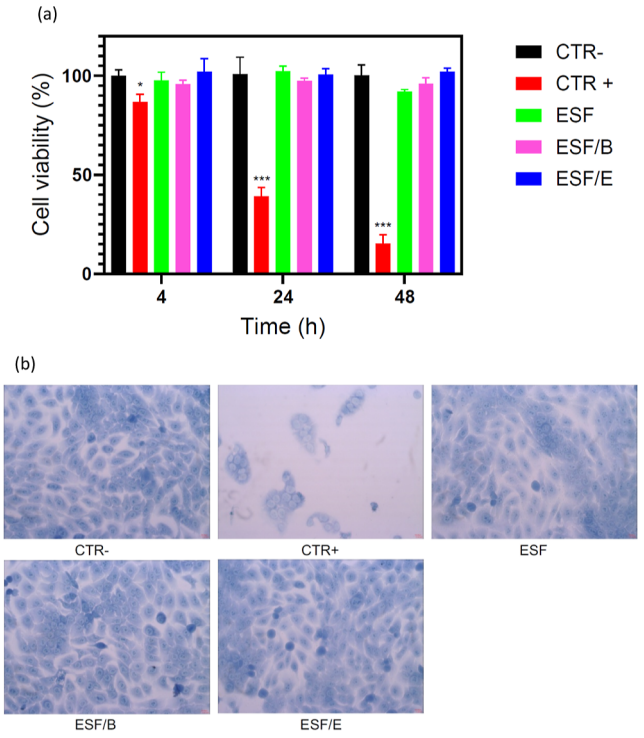

Figure 4. (a) MTT assay on HaCaT cells after 4, 24, and 48 h of 220 s irradiation with the protection of water-vapor-treated ESF, ESF/B, and ESF/E patches. Negative and positive controls were also reported. (b) Optical microscopy images of HaCaT cells after 48 h of 220 s irradiation with the protection of water-vapor-treated ESF, ESF/B, and ESF/E patches. Negative and positive controls were also reported.

The characteristic morphology of silk nanofibers produced by electrospinning after UV sterilization (Figure 5a−c) appears very similar to that observed in Figure 2b, for example, smooth, randomly oriented, and continuous everywhere. The cellularization properties of ESF/E were demonstrated by seeding HaCat cells onto the ESF/E patch. The results clearly revealed that HaCat cells were able not only to grow on the individual fibers but also to populate the spaces between the fibers, indicating their ability to thoroughly cellularize the scaffold. Figure 5d depicts the dense network formed by the growth of keratinocytes and the production of an extracellular matrix, resulting in complete and extensive coverage. The high cell density and interconnectivity make it challenging to distinguish individual cells on the electrospun silk fibers. Figure 5e,f further demonstrate the significant interaction between cells and the substrate surface as well as the interconnectedness among the cells themselves. These findings highlight the favorable cell−scaffold interaction and the establishment of cell−cell interconnections observed in the study.

CONCLUSIONS

In this study, we dissolved salmon sperm DNA in water-soluble silk fibroin that was electrospun into nanofibrous patches through a bioinspired spinning process. Our findings revealed

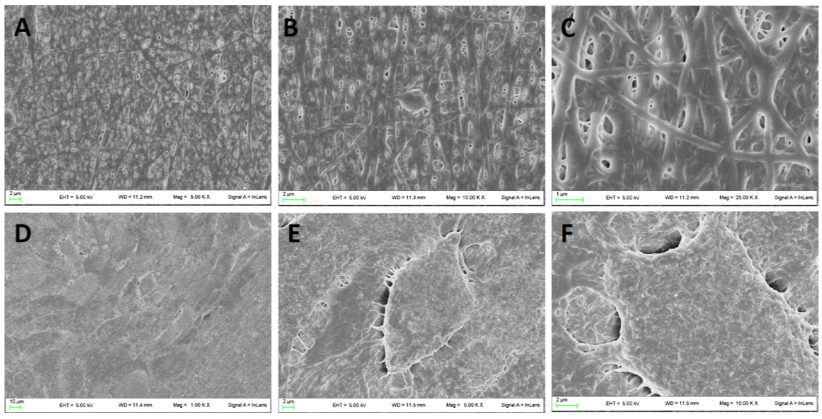

Figure 5. Representative SEM micrographs of electrospun silk fibroin seeded with HaCat cells. (a−c) Negative control of unseeded ESF/E patch displaying typical filamentous texture of electrospun materials at different magnifications. (d−f) ESF/E was seeded with HaCat cells for 24 h. At low magnification, (d) is shown the cell monolayer completely covering the scaffold. Images at high magnification (e and f) show cell membrane protrusions interacting with silk fibroin fibers.

https://doi.org/10.1021/acsomega.3c04563
ACS Omega 2023, 8, 38233−38242

that the incorporation of salmon sperm DNA into SF is effective in producing a UV-blocking patch dressing while maintaining the viability of human keratinocyte HaCaT cells. Additionally, we demonstrated the bidirectional actuation behavior of vapor-responsive patches. These results were interpreted in terms of a synergistic effect of the conformational transition of silk fibroin protein from the α-helix conformation to β-sheets upon vapor exposure and the aggregation of nanofibers, resulting in tighter packing and less porous patches. Finally, our study demonstrates the possibility of exploiting the water insolubility of these films for the growth of HaCaT cells. The ability of the patches to respond bidirectionally together with their capacity to support keratinocyte growth is supported by our results, and it can be also leveraged to create complex shapes for biomedical applications.

■ ASSOCIATED CONTENT

Supporting Information

The Supporting Information is available free of charge at https://pubs.acs.org/doi/10.1021/acsomega.3c04563.

Fitting procedure to estimate the curvature radius for ESF/E patch after water vapor treatment, second derivative of ATR intensity of the ESF sample and comparison between the ATR spectra of DNA and that obtained by subtracting the ESF spectrum from that of ESF/E, water uptake of ESF/E patch after immersion for 1 week in PBS, and evolution of current−voltage curves of ESF electrospun nanofibrous patches upon exposure to water vapor (PDF)

■ AUTHOR INFORMATION

Corresponding Author

Luca Valentini − *Civil and Environmental Engineering Department and INSTM Research Unit, University of Perugia, Terni 05100, Italy;* orcid.org/0000-0002-6803-5889; Email: luca.valentini@unipg.it

Authors

Maria Rachele Ceccarini − *Department of Pharmaceutical Science, University of Perugia, Perugia 06123, Italy*

Irene Chiesa − *Department of Ingegneria dell'Informazione and Research Center E. Piaggio, University of Pisa, Pisa 56122, Italy*

Francesca Ripanti − *Dipartimento di Fisica e Geologia, Università degli Studi di Perugia, Perugia 06123, Italy;* orcid.org/0000-0002-9505-740X

Martina Alunni Cardinali − *Department of Chemistry, Biology and Biotechnology, University of Perugia, Perugia 06123, Italy*

Simone Micalizzi − *Department of Ingegneria dell'Informazione and Research Center E. Piaggio, University of Pisa, Pisa 56122, Italy*

Gabriele Scattini − *Dipartimento di Medicina Veterinaria, University of Perugia, Perugia 06126, Italy*

Carmelo De Maria − *Department of Ingegneria dell'Informazione and Research Center E. Piaggio, University of Pisa, Pisa 56122, Italy;* orcid.org/0000-0002-1368-3571

Alessandro Paciaroni − *Dipartimento di Fisica e Geologia, Università degli Studi di Perugia, Perugia 06123, Italy;* orcid.org/0000-0002-3952-1634

Caterina Petrillo − *Dipartimento di Fisica e Geologia, Università degli Studi di Perugia, Perugia 06123, Italy*

Lucia Comez − *Istituto Officina dei Materiali-IOM, National Research Council-CNR, Perugia 06123, Italy;* orcid.org/0000-0001-5160-6844

Matteo Bertelli − *MAGI'S LAB, Rovereto 38068, Italy*

Paola Sassi − *Department of Chemistry, Biology and Biotechnology, University of Perugia, Perugia 06123, Italy;* orcid.org/0000-0002-4920-2784

Luisa Pascucci − *Dipartimento di Medicina Veterinaria, University of Perugia, Perugia 06126, Italy*

Tommaso Beccari − *Department of Pharmaceutical Science, University of Perugia, Perugia 06123, Italy*

Complete contact information is available at: https://pubs.acs.org/10.1021/acsomega.3c04563

Author Contributions

M.R.C. and I.C. are first coauthors. The manuscript was written with the contributions of all the authors. All the authors have approved the final version of the manuscript. M.R.C., I.C., F.R., M.A.C., G.S., and S.M. were involved in laboratory research; M.R.C., I.C., C.DeM., F.R., L.C., A.P., P.S., L.P., and L.V. wrote the original draft; all the authors revised the original draft. L.V., C.D.M., and T.B. contributed to the conceptualization of experiments, and L.V. contributed to the overall coordination of the research activities. All the authors have read and agreed to the published version of the manuscript.

Funding

L.V., C.D.M., and I.C. received funding from the Italian Ministry of Education, University and Research (MIUR) under the PRIN project "Development and promotion of the Levulinic acid and Carboxylate platforms by the formulation of novel and advanced PHA-based biomaterials and their exploitation for 3D printed green-electronics applications" grant 2017FWC3WC. Research at IOM-CNR, Dipartimento di Science Farmaceutiche, Dipartimento di Fisica e Geologia, Dipartimento di Chimica, Biologia e Biotecnologia and Dipartimento di Ingegneria Civile e Ambientale of the University of Perugia has been funded by the European Union—NextGenerationEU under the Italian Ministry of University and Research (MUR) National Innovation Ecosystem grant ECS00000041—VITALITY. L.V., A.P., L.C., P.S., M.A.C., and T.B. acknowledge Università degli Studi di Perugia and MUR for support within the project Vitality.

Notes

The authors declare no competing financial interest.

■ ACKNOWLEDGMENTS

I.C. and C.D.M. acknowledge the support of the Crosslab Additive Manufacturing of the Department of Information Engineering of the University of Pisa and the support of the FoReLab of the Department of Information Engineering of the University of Pisa.

■ REFERENCES

(1) Vollrath, F.; Knight, D. P. Liquid crystalline spinning of spider silk. *Nature* **2001**, *410* (6828), 541−548.

(2) Jin, H. J.; Kaplan, D. L. Mechanism of silk processing in insects and spiders. *Nature* **2003**, *424* (6952), 1057−1061.

(3) Eisoldt, L.; Smith, A.; Scheibel, T. Decoding the secrets of spider silk. *Mater. Today* **2011**, *14*, 80−86.

(4) Asakura, T.; Umemura, K.; Nakazawa, Y.; Hirose, H.; Higham, J.; Knight, D. Some observations on the structure and function of the spinning apparatus in the silkworm Bombyx mori. *Biomacromolecules* **2007**, *8* (1), 175−181.

(5) Xie, F.; Zhang, H.; Shao, H.; Hu, X. Effect of shearing on formation of silk fibers from regenerated Bombyx mori silk fibroin aqueous solution. *Int. J. Biol. Macromol.* **2006**, *38* (3−5), 284−288.
(6) Peng, Q.; Shao, H.; Hu, X.; Zhang, Y. Role of humidity on the structures and properties of regenerated silk fibers. *Prog. Nat. Sci.: Mater. Int.* **2015**, *25*, 430−436.
(7) Yue, X.; Zhang, F.; Wu, H.; Ming, J.; Fan, Z.; Zuo, B. A novel route to prepare dry-spun silk fibers from CaCl2-formic acid solution. *Mater. Lett.* **2014**, *128*, 175−178.
(8) Luo, J.; Zhang, L.; Peng, Q.; Sun, M.; Zhang, Y.; Shao, H.; Hu, X. Tough silk fibers prepared in air using a biomimetic microfluidic chip. *Int. J. Biol. Macromol.* **2014**, *66*, 319−324.
(9) Wei, W.; Zhang, Y.; Zhao, Y.; Shao, H.; Hu, X. Studies on the post-treatment of the dry-spun fibers from regenerated silk fibroin solution: post-treatment agent and method. *Mater. Des.* **2012**, *36*, 816−822.
(10) Wei, W.; Zhang, Y.; Shao, H.; Hu, X. Post-treatment of the dry-spun fibers obtained from regenerated silk fibroin aqueous solution in ethanol aqueous solution. *J. Mater. Res.* **2011**, *26*, 1100−1106.
(11) Wei, W.; Zhang, Y.; Zhao, Y.; Luo, J.; Shao, H.; Hu, X. Bio-inspired capillary dry spinning of regenerated silk fibroin aqueous solution. *Mater. Sci. Eng., C* **2011**, *31* (7), 1602−1608.
(12) Jin, Y.; Zhang, Y.; Hang, Y.; Shao, H.; Hu, X. A simple process for dry spinning of regenerated silk fibroin aqueous solution. *J. Mater. Res.* **2013**, *28*, 2897−2902.
(13) Sun, M.; Zhang, Y.; Zhao, Y.; Shao, H.; Hu, X. The structure-property relationships of artificial silk fabricated by dry-spinning process. *J. Mater. Chem.* **2012**, *22*, 18372−18379.
(14) Bell, F.; McEwen, I.; Viney, C. Supercontraction stress in wet spider dragline. *Nature* **2002**, *416*, 37.
(15) Agnarsson, I.; Dhinojwala, A.; Sahni, V.; Blackledge, T. A. Spider silk as a novel high performance biomimetic muscle driven by humidity. *J. Exp. Biol.* **2009**, *212* (13), 1990−1994.
(16) Blackledge, T. A.; Boutry, C.; Wong, S. C.; Baji, A.; Dhinojwala, A.; Sahni, V.; Agnarsson, I. How super is supercontraction? Persistent versus cyclic responses to humidity in spider dragline silk. *J. Exp. Biol.* **2009**, *212* (13), 1981−1989.
(17) Guan, J.; Vollrath, F.; Porter, D. Two mechanisms for supercontraction in Nephila spider dragline silk. *Biomacromolecules* **2011**, *12* (11), 4030−4035.
(18) Gosline, J. M.; Guerette, P. A.; Ortlepp, C. S.; Savage, K. N. The mechanical design of spider silks: from fibroin sequence to mechanical function. *J. Exp. Biol.* **1999**, *202* (23), 3295−3303.
(19) Blamires, S. J.; Rawal, A.; Edwards, A. D.; Yarger, J. L.; Oberst, S.; Allardyce, B. J.; Rajkhowa, R. Methods for Silk Property Analyses across Structural Hierarchies and Scales. *Molecules* **2023**, *28*, 2120.
(20) Giesa, T.; Schuetz, R.; Fratzl, P.; Buehler, M. J.; Masic, A. Unraveling the Molecular Requirements for Macroscopic Silk Supercontraction. *ACS Nano* **2017**, *11* (10), 9750−9758.
(21) Ube, T. Development of novel network structures in crosslinked liquid-crystalline polymers. *Polym. J.* **2019**, *51*, 983−988 (2019).
(22) Hippler, M.; Blasco, E.; Qu, J.; Tanaka, M.; Barner-Kowollik, C.; Wegener, M.; Bastmeyer, M. Controlling the shape of 3D microstructures by temperature and light. *Nat. Commun.* **2019**, *10* (1), 232.
(23) Zhao, Q.; Dunlop, J. W.; Qiu, X.; Huang, F.; Zhang, Z.; Heyda, J.; Dzubiella, J.; Antonietti, M.; Yuan, J. An instant multi-responsive porous polymer actuator driven by solvent molecule sorption. *Nat. Commun.* **2014**, *5*, 4293.
(24) Mu, J.; Hou, C.; Zhu, B.; Wang, H.; Li, Y.; Zhang, Q. A multi-responsive water-driven actuator with instant and powerful performance for versatile applications. *Sci. Rep.* **2015**, *5*, 9503.
(25) Mu, J.; Wang, G.; Yan, H.; Li, H.; Wang, X.; Gao, E.; Hou, C.; Pham, A. T. C.; Wu, L.; Zhang, Q.; Li, Y.; Xu, Z.; Guo, Y.; Reichmanis, E.; Wang, H.; Zhu, M. Molecular-channel driven actuator with considerations for multiple configurations and color switching. *Nat. Commun.* **2018**, *9* (1), 590.
(26) Wang, T.; Li, M.; Zhang, H.; Sun, Y.; Dong, B. A multiresponsive bidirectional bending actuator based on polypyrrole and agar nanocomposites. *J. Mater. Chem. C* **2018**, *6*, 6416−6422.
(27) Dong, Y.; Wang, J.; Guo, X.; Yang, S.; Ozen, M. O.; Chen, P.; Liu, X.; Du, W.; Xiao, F.; Demirci, U.; Liu, B. F. Multi-stimuli-responsive programmable biomimetic actuator. *Nat. Commun.* **2019**, *10* (1), 4087.
(28) Zhang, Y. L.; Ma, J. N.; Liu, S.; Han, D. D.; Liu, Y. Q.; Chen, Z. D.; Mao, J. W.; Sun, H. B. A "Yin"-"Yang" complementarity strategy for design and fabrication of dual-responsive bimorph actuators. *Nano Energy* **2020**, *68*, 104302.
(29) Manikandan, G.; Murali, A.; Kumar, R.; Satapathy, D. K. Rapid Moisture-Responsive Silk Fibroin Actuators. *ACS Appl. Mater. Interfaces* **2021**, *13* (7), 8880−8888.
(30) Sinn, G.; Fizek, E.; Wimmer, R.; Lichtenegger, H. Mechanics of a Biomimetic Moisture Sensitive Actuator Based on Compression Wood. *Polymers* **2022**, *14*, 1624.
(31) Jamal, M.; Kadam, S. S.; Xiao, R.; Jivan, F.; Onn, T. M.; Fernandes, R.; Nguyen, T. D.; Gracias, D. H. Bio-origami hydrogel scaffolds composed of photocrosslinked PEG bilayers. *Adv. Healthcare Mater.* **2013**, *2* (8), 1142−1150.
(32) Gasperini, A. E.; Sanchez, S.; Doiron, A. L.; Lyles, M.; German, G. K. Non-ionising UV light increases the optical density of hygroscopic self assembled DNA crystal films. *Sci. Rep.* **2017**, *7* (1), 6631.
(33) Han, J.; Cui, Y.; Han, X.; Liang, C.; Liu, W.; Luo, D.; Yang, D. Super-Soft DNA/Dopamine-Grafted-Dextran Hydrogel as Dynamic Wire for Electric Circuits Switched by a Microbial Metabolism Process. *Adv. Sci.* **2020**, *7* (13), 2000684.
(34) Tang, J.; Yao, C.; Gu, Z.; Jung, S.; Luo, D.; Yang, D. Super-Soft and Super-Elastic DNA Robot with Magnetically Driven Navigational Locomotion for Cell Delivery in Confined Space. *Angew. Chem., Int. Ed. Engl.* **2020**, *59* (6), 2490−2495.
(35) Ceccarini, M. R.; Ripanti, F.; Raggi, V.; Paciaroni, A.; Petrillo, C.; Comez, L.; Donato, K.; Bertelli, M.; Beccari, T.; Valentini, L. Development of Salmon Sperm DNA/Regenerated Silk Bio-Based Films for Biomedical Studies on Human Keratinocyte HaCaT Cells under Solar Spectrum. *J. Funct. Biomater.* **2023**, *14* (5), 280.
(36) Keten, S.; Xu, Z.; Ihle, B.; Buehler, M. J. Nanoconfinement controls stiffness, strength and mechanical toughness of beta-sheet crystals in silk. *Nat. Mater.* **2010**, *9* (4), 359−367.
(37) Zhang, F.; Zuo, B.; Fan, Z.; Xie, Z.; Lu, Q.; Zhang, X.; Kaplan, D. L. Mechanisms and control of silk-based electrospinning. *Biomacromolecules* **2012**, *13* (3), 798−804.
(38) Rockwood, D. N.; Preda, R. C.; Yücel, T.; Wang, X.; Lovett, M. L.; Kaplan, D. L. Materials fabrication from Bombyx mori silk fibroin. *Nat. Protoc.* **2011**, *6* (10), 1612−1631.
(39) Sionkowska, A.; Płanecka, A.; Lewandowska, K.; Michalska, M. The influence of UV-irradiation on thermal and mechanical properties of chitosan and silk fibroin mixtures. *J. Photochem. Photobiol., B* **2014**, *140*, 301−305.
(40) Li, X.-G.; Wu, L.-Y.; Huang, M.-R.; Shao, H.-L.; Hu, X.-C. Conformational transition and liquid crystalline state of regenerated silk fibroin in water. *Biopolymers* **2008**, *89*, 497−505.
(41) Keten, S.; Xu, Z.; Ihle, B.; Buehler, M. J. Nanoconfinement controls stiffness, strength and mechanical toughness of beta-sheet crystals in silk. *Nat. Mater.* **2010**, *9* (4), 359−367.
(42) van Beek, J. D.; Hess, S.; Vollrath, F.; Meier, B. H. The molecular structure of spider dragline silk: folding and orientation of the protein backbone. *Proc. Natl. Acad. Sci. U.S.A.* **2002**, *99* (16), 10266−10271.
(43) Asakura, T. Structure of Silk I (*Bombyx mori* Silk Fibroin before Spinning) -Type II β-Turn, Not α-Helix-. *Molecules* **2021**, *26*, 3706.
(44) Kong, J.; Yu, S. Fourier transform infrared spectroscopic analysis of protein secondary structures. *Acta Biochim. Biophys. Sin.* **2007**, *39*, 549−559.
(45) Nowak, E.; Wisła-Świder, A.; Khachatryan, G.; Fiedorowicz, M.; Danel, K. Possible sensor applications of selected DNA-surfactant complexes. *Eur. Biophys. J.* **2019**, *48*, 371−381.
(46) Mello, M. L. S.; Vidal, B. C. Changes in the infrared microspectroscopic characteristics of dna caused by cationic elements, different base richness and single-stranded form. *PLoS One* **2012**, *7*, No. e43169.
(47) Ionov, L. Biomimetic hydrogel-based actuating systems. *Adv. Funct. Mater.* **2013**, *23*, 4555−4570.

https://doi.org/10.1021/acsomega.3c04563
ACS Omega 2023, 8, 38233−38242

(48) Rath, A.; Geethu, P. M.; Mathesan, S.; Satapathy, D. K.; Ghosh, P. Solvent triggered irreversible shape morphism of biopolymer films. *Soft Matter* **2018**, *14* (9), 1672−1680.
(49) Castaldo, R.; Lama, G. C.; Aprea, P.; Gentile, G.; Ambrogi, V.; Lavorgna, M.; Cerruti, P. Humidity-Driven Mechanical and Electrical Response of Graphene/Cloisite Hybrid Films. *Adv. Funct. Mater.* **2019**, *29*, 1807744.
(50) Li, G.; Tian, Q.; Wu, W.; Yang, S.; Wu, Q.; Zhao, Y.; Wang, J.; Zhou, X.; Wang, K.; Ren, L.; et al. Bio-Inspired 4D Printing of Dynamic Spider Silks. *Polymers* **2022**, *14*, 2069.
(51) Su, I.; Buehler, M. J. Mesomechanics of a three-dimensional spider web. *J. Mech. Phys. Solid.* **2020**, *144*, 104096.
(52) Lu, Q.; Hu, X.; Wang, X.; Kluge, J. A.; Lu, S.; Cebe, P.; Kaplan, D. L. Water-insoluble silk films with silk I structure. *Acta Biomater.* **2010**, *6* (4), 1380−1387.
(53) Affanni, A.; Corazza, A.; Esposito, G.; Fogolari, F.; Polano, M. Protein aggregation measurement through electrical impedance spectroscopy. *J. Phys.: Conf. Ser.* **2013**, *459*, 012049.
(54) Hudson, L.; Rashdan, E.; Bonn, C. A.; Chavan, B.; Rawlings, D.; Birch-Machin, M. A. Individual and combined effects of the infrared, visible, and ultraviolet light components of solar radiation on damage biomarkers in human skin cells. *FASEB J.* **2020**, *34* (3), 3874−3883.
(55) Bowman, A.; Birch-Machin, M. A. Mitochondrial DNA as a Sensitive Biomarker of UV-Induced Cellular Damage in Human Skin. *Methods Mol. Biol.* **2021**, *2277*, 345−356.
(56) Plitta-Michalak, B.; Stricker, N.; Pavez Loriè, E.; Chen, I.; Pollet, M.; Krutmann, J.; Volkmer, B.; Greinert, R.; Boukamp, P.; Rapp, A. Development and characterisation of an irradiation device for biomedical studies covering the solar spectrum with individual regulated spectral bands. *Photochem. Photobiol. Sci.* **2022**, *21* (9), 1701−1717.
(57) Poquet, L.; Clifford, M. N.; Williamson, G. Effect of dihydrocaffeic acid on UV irradiation of human keratinocyte HaCaT cells. *Arch. Biochem. Biophys.* **2008**, *476* (2), 196−204.

https://doi.org/10.1021/acsomega.3c04563
ACS Omega 2023, 8, 38233−38242